

# Entangling lattice-trapped bosons with a free impurity: impact on stationary and dynamical properties

Maxim Pyzh,<sup>1,\*</sup> Kevin Keiler,<sup>1</sup> Simeon I. Mistakidis,<sup>1</sup> and Peter Schmelcher<sup>1,2,†</sup>

<sup>1</sup>*Center for Optical Quantum Technologies, Department of Physics,  
University of Hamburg, Luruper Chaussee 149, 22761 Hamburg Germany*

<sup>2</sup>*The Hamburg Centre for Ultrafast Imaging, Universität Hamburg,  
Luruper Chaussee 149, 22761 Hamburg, Germany*

We address the interplay of few lattice trapped bosons interacting with an impurity atom in a box potential. For the ground state, a classification is performed based on the fidelity allowing to quantify the susceptibility of the composite system to structural changes due to the intercomponent coupling. We analyze the overall response at the many-body level and contrast it to the single-particle level. By inspecting different entropy measures we capture the degree of entanglement and intraspecies correlations for a wide range of intra- and intercomponent interactions and lattice depths. We also spatially resolve the imprint of the entanglement on the one- and two-body density distributions showcasing that it accelerates the phase separation process or acts against spatial localization for repulsive and attractive intercomponent interactions respectively. The many-body effects on the tunneling dynamics of the individual components, resulting from their counterflow, are also discussed. The tunneling period of the impurity is very sensitive to the value of the impurity-medium coupling due to its effective dressing by the few-body medium. Our work provides implications for engineering localized structures in correlated impurity settings using species selective optical potentials.

## I. INTRODUCTION

Multicomponent quantum gases can be experimentally studied with a high degree of controllability in the ultra-cold regime [1, 2]. Specifically, two-component mixtures of bosons or fermions can be trapped in various species selective external geometries [3, 4]. Few-body ensembles can be realized in particular in one-dimension (1D) [5, 6] while the scattering lengths are tunable through Feshbach and confinement induced resonances [7, 8]. In 1D bosonic mixtures the adjustability of the intercomponent interactions gives rise to intriguing phenomena such as phase-separation processes [9, 10] in the repulsive regime, formation of bound states, e.g., droplet configurations [11, 12] for attractive interactions as well as quasiparticle-like states in highly particle imbalanced systems [13, 14].

In this latter context, an impurity species is embedded in an environment of the majority species called the medium. The presence of a finite impurity-medium coupling leads to an effective picture where the impurity properties deviate from the bare particle case exhibiting, for instance, an effective mass [15–18] and induced interactions [19–22] mediated by the medium. The resultant states are often called polarons [23, 24] and have been experimentally realized mainly in higher-dimensions [25–29] and to a lesser extent in 1D [13, 30] using spectroscopic schemes. Since these settings consist of a few-body subsystem they naturally show enhanced correlation properties, especially in 1D, rendering their many-body treatment inevitable. In particular, the emergent

impurity-medium entanglement can lead to spatial undulations of the medium. This mechanism is manifested, for instance, as sound-wave emission [17, 31] and collective excitations [32, 33] of the host or the formation of a bound state [34–36] between the impurity and atoms of the medium for attractive interspecies interactions.

Another relevant ingredient is the external trapping geometry that the two components experience. Indeed, for harmonically trapped and homogeneous systems remarkable dynamical features of impurity physics include the spontaneous generation of localized patterns [17, 37, 38], inelastic collisional aspects of driven impurities [39–41] with the surrounding and their relaxation at long timescales [42–44]. On the other hand, when a lattice potential is introduced the situation becomes more complicated giving rise, among others, to doped insulator physics [45, 46] and impurity transport [47–49]. Apparently, configuring one component by manipulating its external trap while leaving the other intact, e.g. by using a species selective external potential, it is possible to control the response of the unperturbed component via the impurity-medium interaction [50, 51]. For instance, operating in the lowest-band approximation it has been demonstrated that a lattice trapped impurity interacting with a homogeneous host exhibits besides tunneling dynamics [52] also self-trapping events [53, 54] and can even undergo Bloch-oscillations [55]. The opposite case, where the medium resides in the lattice, provides an experimental probe of the impurity-medium collision parameters [56] and interaction strength [57].

In this work by considering an impurity in a box potential and a lattice trapped few-body medium we examine how the latter affects the impurity’s spatial distribution by means of (de-)localization for different lattice depths and intercomponent interactions. Indeed, a lat-

\* mpyzh@physnet.uni-hamburg.de

† pschmelc@physnet.uni-hamburg.de

tice trapped medium can reside either in a superfluid or an insulating-like phase [45], a fact that is expected to crucially impact the impurity's configuration and vice versa [58]. To address the ground state properties and quantum quench dynamics of the above-discussed impurity setting we utilize the multi-layer multi-configuration time-dependent Hartree method for atomic mixtures (ML-MCTDHF) [59–61]. This variational method enables us to account for the relevant correlations of the mixture and operate beyond the lowest-band approximation for the medium.

Focusing on the ground state of the system and in order to testify its overall response for varying intercomponent interactions we determine the fidelity between the coupled and decoupled composite system both at the many-body and the single-particle level. Note that in impurity settings this observable is commonly termed residue [23, 24] enabling us to identify e.g. the polaron formation, while the influence of the impurity-medium entanglement in this observable is still an open issue. It is demonstrated that despite the fact that the total entangled state may strongly deviate from its decoupled configuration, this effect is arguably less pronounced or even diminished at the single-particle level. Furthermore, we showcase that the build-up of impurity-medium entanglement is sensitive to the interplay between the intercomponent interactions and the lattice depth [45]. Interestingly, stronger interactions do not necessarily lead to a larger amount of entanglement, whereas the state of the majority species may undergo substantial structural changes, which remain invisible at the single-particle level. Moreover, we identify the imprint of the background on the impurities and vice versa by relying on one- and two-body density distributions evincing a rich spatial structure of the components with respect to the lattice depth as well as the inter- and intracomponent interactions. In particular, it is argued that for repulsive (attractive) interactions the impurity delocalizes (localizes) around the central lattice site. The delocalization of the impurity is accompanied by its phase-separation with the majority component [62], where the impurity tends to the edges of the box for a superfluid background or exhibits a multi-hump structure for an insulating medium. We further analyze how much the intercomponent correlations are actually involved in the structural changes observed in the spatial probability distributions. To this end we compare density distributions of the numerically exact ground state to the corresponding ones of an approximate non-entangled ground state. We identify that the entanglement-induced corrections accelerate phase-separation at repulsive couplings and generally slow down spatial localization at attractive interactions.

Finally, we monitor the non-equilibrium dynamics of the mixture. We prepare the system in a phase-separated, i.e. disentangled configuration, and quench the intercomponent interactions to smaller values resulting in the counterflow of the components and thus triggering their tunneling dynamics and the consequent

build-up of entanglement. The majority component plays the role of a material barrier for the impurity [49, 63] which performs tunneling oscillations whose period depends strongly on the impurity-medium interaction. The many-body nature of the tunneling process of the components is testified by invoking the individual natural orbitals constituting the time-evolved many-body state.

Our presentation is structured as follows. In Section II we introduce the impurity setting and in Section III we discuss our many-body treatment to tackle its ground state and dynamics. The ground state properties of the delocalized impurity and the lattice trapped medium are addressed in Section IV. We analyze the fidelity between perturbed and unperturbed (reduced) density operators, quantify the degree of entanglement and visualize its impact on single- and two-body density distributions of each species for different intra- and intercomponent interactions and lattice depths. The non-equilibrium dynamics of the mixture following a quench of the impurity-medium coupling to smaller values is discussed in Section V. We provide a summary of our results and elaborate on future perspectives in Section VI.

## II. SETUP AND HAMILTONIAN

We consider a single impurity particle immersed in a few-body system of ultracold bosons. Both components reside in a quasi-1D geometry ensured by a strong transversal confinement [13]. Along the longitudinal direction the  $N_A$  majority species atoms of mass  $m_A$  are trapped inside a lattice of depth  $V$  with  $l$  sites and length  $L$  with hard-wall boundary conditions. The impurity atom of mass  $m_B$  is subject to a box potential of the same length. The species-dependent trapping has been successfully demonstrated experimentally [3, 4]. The interparticle interactions are of s-wave contact type with  $g_{AA}$  denoting the majority-majority interaction strength and  $g_{AB}$  the majority-impurity coupling. Both may be tuned independently by a combination of Feshbach and confinement induced resonances [7, 8]. Furthermore, we assume equal masses  $m_A = m_B$ , which corresponds to a mixture of the same isotope with the particles being distinguishable due to two different hyperfine states [64–69]. By introducing  $R^* = L$  and  $E^* = \hbar^2/(mL^2)$  as length and energy scales we arrive at the following rescaled many-body Hamiltonian:

$$H = -\frac{1}{2} \frac{\partial^2}{\partial y^2} - \sum_i^{N_A} \left( \frac{1}{2} \frac{\partial^2}{\partial x_i^2} + V \sin^2(\pi l x_i) \right) + g_{AA} \sum_{i < j}^{N_A} \delta(x_i - x_j) + g_{AB} \sum_i^{N_A} \delta(x_i - y), \quad (1)$$

where  $y$  and  $x_i$  denote the spatial coordinates of the impurity and  $i$ th majority atom respectively.

In this work we primarily focus on the ground state properties of the above many-body Hamiltonian Eq. (1)

with  $l = 5$  lattice sites and  $N_A = 5$  majority particles. In particular, we are interested in the susceptibility of the composite system to structural changes and the amount of inter-particle correlations it may hold. We cover a parameter space from moderately attractive to repulsive interaction strengths, i.e.,  $g_{AA} \in [-3.0, 3.0] E^* R^*$  and  $g_{AB} \in [-5.0, 5.0] E^* R^*$ , for a range of lattice depths from shallow to deep, namely  $V \in [100, 1000] E^*$ . In the following, we will refer to a lattice as being shallow ( $V < 200$ ), moderately deep ( $V \approx 500$ ) and very deep ( $V > 800$ ). Additionally, we demonstrate how an initially disentangled state prepared in the immiscible regime acquires dynamically a finite amount of entanglement after quenching the intercomponent coupling  $g_{AB}$ , thus triggering a counter-flow tunneling process of the two components.

### III. VARIATIONAL APPROACH

In order to account for effects stemming from inter-particle correlations we rely on the Multi-Layer Multi-Configurational Time-Dependent Hartree Method for atomic mixtures (ML-MCTDHX), for short ML-X [59–61]. This ab-initio method has been successfully applied to solve the time-dependent Schrödinger equation of various experimentally accessible and extensively studied systems. The core idea of this method lies in expanding the many-body wave-function in terms of product states of *time-dependent* single-particle functions [70, 71]. This becomes beneficial, when the number of basis configurations with considerable contribution to the state fluctuates weakly during the time propagation, whereas the configurations themselves do change. Taking a variationally optimal basis at each time-step allows us to cover the high-dimensional Hilbert space at a lower computational cost compared to a time-independent basis.

The wave function ansatz for a given system is decomposed in multiple layers. On the first layer, called top layer, we separate the degrees of freedom of the binary mixture into product states of majority and impurity species functions  $|\Psi_i^\sigma(t)\rangle$  with  $\sigma \in \{A, B\}$  and  $i \in \{1, \dots, S\}$ :

$$|\Psi(t)\rangle = \sum_{i=1}^S \sqrt{\lambda_i(t)} |\Psi_i^A(t)\rangle \otimes |\Psi_i^B(t)\rangle. \quad (2)$$

Here, the time-dependent coefficients  $\lambda_i(t)$ , normalized as  $\sum_{i=1}^S \lambda_i(t) = 1$ , determine the degree of entanglement between the components [72]. The choice of  $S = 1$  results in the so-called species mean-field (SMF) approximation, meaning that no entanglement is assumed between the components [15]. In that case the intercomponent correlations, if present, are neglected and every component is effectively subject to an additional one-body potential induced by the fellow species [49, 62]. In this work, we put a special emphasis on the impact of the entanglement on several one- and two-body quantities by comparing

the numerically exact ground state to the corresponding SMF approximation.

On the second layer, called species layer, each species function  $|\Psi_i^\sigma(t)\rangle$  is expanded in terms of species-dependent symmetrized product states of single-particle functions (SPFs)  $|\varphi_j^\sigma(t)\rangle$  with  $j \in \{1, \dots, s_\sigma\}$ , accounting for the bosonic nature of our particles and abbreviated as  $|\vec{n}^\sigma\rangle = |n_1^\sigma, \dots, n_{s_\sigma}^\sigma\rangle$ :

$$|\Psi_i^\sigma(t)\rangle = \sum_{\vec{n}^\sigma | N_\sigma} C_{i, \vec{n}^\sigma}(t) |\vec{n}^\sigma(t)\rangle. \quad (3)$$

In this expression the sum is performed over all configurations  $\vec{n}^\sigma | N_\sigma$  obeying the particle-number constraint  $\sum_{i=1}^{s_\sigma} n_i^\sigma = N_\sigma$ . On the third and final layer, called primitive layer, each SPF is represented on a one-dimensional time-independent grid [73].

The Dirac-Frenkel variational principle [74] is subsequently applied to the above ansatz in order to derive the coupled equations of motion for the expansion coefficients  $\lambda_i(t)$ ,  $C_{i, \vec{n}^\sigma}(t)$  and the SPFs  $|\varphi_j^\sigma(t)\rangle$ . Finally, performing imaginary time-evolution one arrives at the ground state wave-function (Section IV), whereas the real time-propagation allows to study the non-equilibrium dynamics of an arbitrary initial state (Section V). The results to be presented below have been obtained by using  $(S, s_A, s_B) = (4, 5, 4)$  functions/SPFs on the top/species layers as well as 225 grid points on the primitive layer. We have carefully checked the convergence behavior of our results by comparing to simulations with a larger number of orbitals  $(S, s_A, s_B) = (6, 8, 6)$  and found no significant changes for the quantities of interest.

In the following we will often refer to the reduced  $j$ -body density operators  $\hat{\rho}_j^\sigma$  of species  $\sigma$  and the intercomponent reduced  $(j+k)$ -body density operator  $\hat{\rho}_{j+k}^{\sigma\bar{\sigma}}$  obtained from the many-body density operator  $\hat{\rho} = |\Psi\rangle\langle\Psi|$ :

$$\hat{\rho}_j^\sigma = \text{tr}_{N_\sigma \setminus j} \{ \text{tr}_{N_{\bar{\sigma}}} \{ \hat{\rho} \} \}, \quad (4)$$

$$\hat{\rho}_{j+k}^{\sigma\bar{\sigma}} = \text{tr}_{N_\sigma \setminus j} \{ \text{tr}_{N_{\bar{\sigma}} \setminus k} \{ \hat{\rho} \} \}, \quad (5)$$

where  $N_\sigma \setminus j$  stands for integrating out  $N_\sigma - j$  coordinates of component  $\sigma$  and  $\bar{\sigma} \neq \sigma$ . Of particular interest are the reduced one-body density operators  $\hat{\rho}_1^A$  and  $\hat{\rho}_1^B$  as well as the reduced two-body intra- and intercomponent density operators  $\hat{\rho}_2^A$  and  $\hat{\rho}_2^{AB}$  respectively, since they determine the expectation values of various experimentally accessible local one- and two-body observables, such as the average particle position, the inter-atomic distance or the wave-packet width.

### IV. IMPACT OF INTERCOMPONENT COUPLING ON GROUND STATE PROPERTIES

In Section IV A we analyze to which extent the many-body wave-function as well as the reduced one-body density operators are modified by the intercomponent interaction. To this end we analyze the fidelity between the

interacting and non-interacting (reduced) density operators, which is a measure of their closeness. We find that with increasing absolute value of the interaction strength the system is more robust w.r.t. changes on the one-body as compared to the many-body level. Moreover, each component is affected differently depending on the lattice depth and majority interaction strength.

Subsequently, in Section IV B we quantify the degree of entanglement by means of the von-Neumann entropy and identify parameter regions with substantial inter-particle correlations. Interestingly, increasing the absolute value of the intercomponent coupling does not always result in stronger entanglement. In fact, there are parameter regions where a strongly interacting ground state becomes almost orthogonal to the non-interacting one and the components remain to a good approximation disentangled.

Finally, we combine insights from Sections IV A and IV B to identify interesting parameter regimes and perform an in-depth analysis of the underlying physical phenomena in Section IV C. In particular, we inspect how the spatial representation of density operators is altered and compare those to the corresponding SMF results. The latter allows us to spatially resolve the corrections to the SMF densities induced by the entanglement and interpret its impact as acceleration or deceleration of the undergoing processes, e.g., the phase separation or localization.

#### A. Fidelity for quantifying the impact of the intercomponent interaction

First, we aim to analyze how the intercomponent coupling  $g_{AB}$  impacts the ground state of non-interacting species (NIS) at  $g_{AB} = 0$ . For this purpose, we evaluate the fidelity [75] of two density operators  $\hat{\rho}$  and  $\hat{\sigma}$  defined as:

$$F(\hat{\rho}, \hat{\sigma}) = \left( \text{tr} \sqrt{\sqrt{\hat{\rho}} \hat{\sigma} \sqrt{\hat{\rho}}} \right)^2 = F(\hat{\sigma}, \hat{\rho}). \quad (6)$$

We start with the fidelity between a NIS many-body density  $\hat{\rho}_0 = |\Psi_0\rangle\langle\Psi_0|$  and a many-body density  $\hat{\rho}_g = |\Psi_g\rangle\langle\Psi_g|$  for some finite coupling  $g_{AB}$  (Fig. 1). Since both density operators describe pure states, Eq. (6) reduces to  $F_{mb} = |\langle\Psi_0|\Psi_g\rangle|^2$ . This measure,  $F_{mb}$ , is also known as the polaron residue studied in the context of phonon dressing of an impurity particle immersed in a bath of majority atoms [23, 24].

For a weakly interacting ( $g_{AA} = 0.5$ ) majority component [Fig. 1a] we observe that the many-body fidelity at a fixed lattice depth decreases monotonously with the modulus of the coupling strength  $g_{AB}$ . At deep lattices the rate of its reduction is larger, a behavior which is even more pronounced at strong negative  $g_{AB}$ , where the interacting state becomes almost orthogonal to the non-interacting one ( $g_{AB} = -5$  and  $V = 1000$ ). The

black dashed line encircles a parameter region of instability where the SMF ansatz collapses to a configuration with broken parity symmetry. For a moderately interacting ( $g_{AA} = 3.0$ ) majority component [Fig. 1b] the many-body fidelity becomes much more stable. Contrarily to Fig. 1a the rate of reduction with  $g_{AB}$  is larger at shallow lattices instead. Finally, for a moderately deep ( $V = 500$ ) lattice [Fig. 1c] we observe a peculiar fast decay around  $g_{AA} \approx -1$  starting at  $g_{AB} < -2$ . Additionally, at  $g_{AA} \approx -1$  and positive  $g_{AB}$  there is a small pronounced decay region (black dashed circle), which is absent in the SMF approximation.

Next, we analyze the fidelity between a free impurity described by a pure state  $|\Phi_0\rangle\langle\Phi_0|$  and an entangled one  $\hat{\rho}_1^B$ , in general being a mixed state [Fig. 2]. Eq. (6) then simplifies to  $F_1^B = |\langle\Phi_0|\hat{\rho}_1^B|\Phi_0\rangle|^2$ . This measure allows to judge to which extent the impurity atom is still a "free" particle of mass  $m_B$ . We emphasize that it should not be confused with a polaron quasi-particle having a renormalized effective mass. We observe that  $F_1^B$  follows overall a similar pattern as the many-body fidelity  $F_{mb}$ , but with a significantly slower decay rate. Though there are some strong qualitative differences, see in particular Fig. 2c. Namely, the abrupt decay of  $F_{mb}$  around  $g_{AA} \approx -1$  at negative  $g_{AB}$  [Fig. 1c] is absent in  $F_1^B$  along with the small decay region at positive  $g_{AB}$  (black dashed circle). From this we anticipate that the majority component is responsible for these features in  $F_{mb}$ .

For the above reason, we now investigate the complementary fidelity  $F_1^A = F(\hat{\rho}_1^A(g_{AB} = 0), \hat{\rho}_1^A)$ , i.e., between mixed states characterizing a majority particle in the NIS state  $\hat{\rho}_1^A(g_{AB} = 0)$  and in the interacting state  $\hat{\rho}_1^A$  [Fig. 3]. This quantity captures to which extent a majority particle is still in a mixed state induced solely by the intraspecies interaction strength  $g_{AA}$ . In case of a weak  $g_{AA}$  [Fig. 3a]  $F_1^A$  is notably affected only at deep lattices  $V > 600$  and strong negative coupling  $g_{AB} < -4$ . For large  $g_{AA}$  [Fig. 3b] we observe that the intercomponent correlations are not strong enough to overcome the intraspecies ones, thus barely affecting the mixedness of the NIS majority state, since  $F_1^A \approx 1$  in the whole range  $-2 < g_{AB} < 5$  and  $100 < V < 700$ . In Fig. 3c we find evidence that the majority component is indeed responsible for the particular decay patterns observed in the many-body fidelity  $F_{mb}$ , which were absent in  $F_1^B$ . Overall, the majority component demonstrates a higher level of robustness at the single-particle level as compared to the impurity.



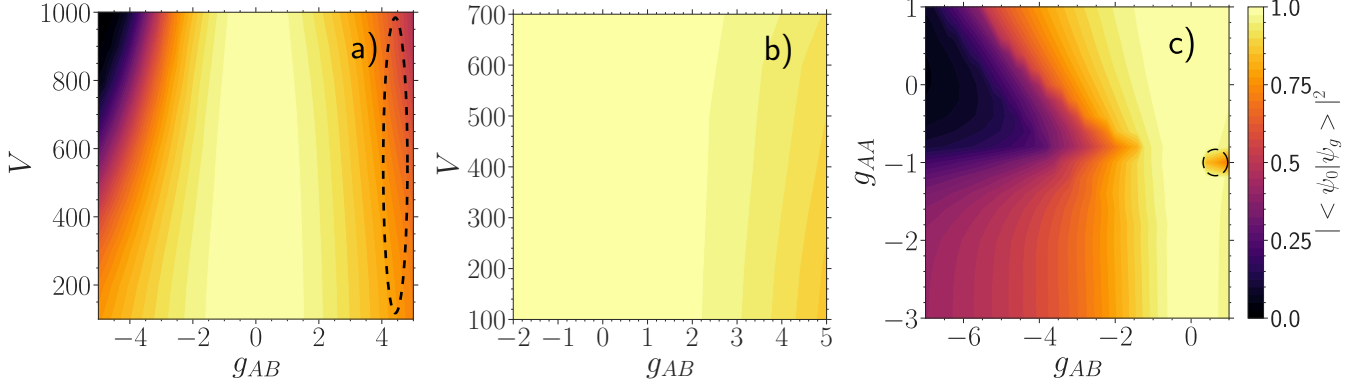


Figure 1. Fidelity  $|\langle \Psi_0 | \Psi_g \rangle|^2$  between a many-body state  $|\Psi_0\rangle$  at  $g_{AB} = 0$  and a many-body one  $|\Psi_g\rangle$  at finite  $g_{AB}$ , for a)  $g_{AA} = 0.5$ , b)  $g_{AA} = 3.0$  and c)  $V = 500$  as a function of the majority-impurity coupling  $g_{AB}$  and the lattice depth  $V$  (a,b) or the interaction strength of the majority atoms  $g_{AA}$  (c). All quantities are given in box units with characteristic length  $R^* = L$  and energy  $E^* = \hbar^2/(mL^2)$  with  $L$  denoting the extension of the box trap. Regions encircled by black dashed lines indicate parameter regions with substantial qualitative differences to the SMF ansatz.

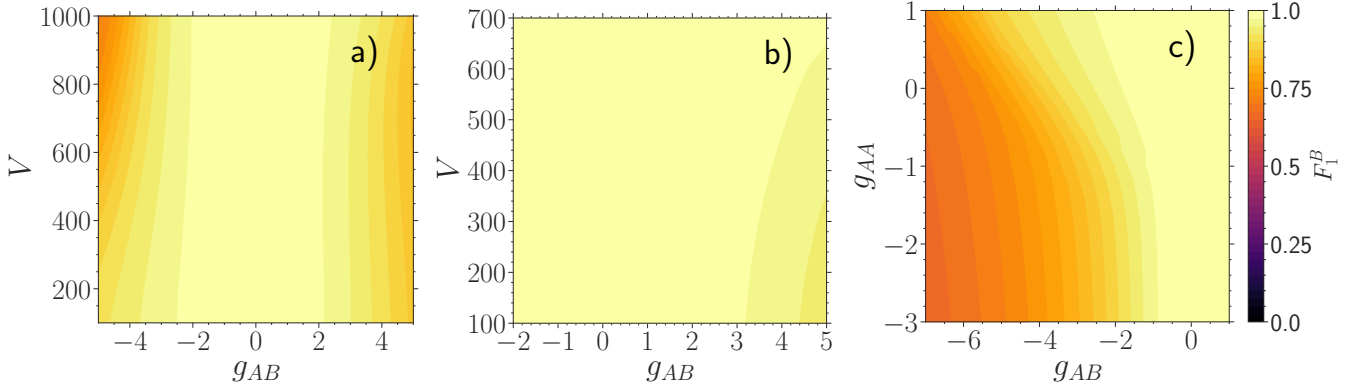


Figure 2. Fidelity  $F_1^B = |\langle \Phi_0 | \hat{\rho}_1^B | \Phi_0 \rangle|^2$  between a free impurity particle  $|\Phi_0\rangle$  at  $g_{AB} = 0$  and an entangled one  $\hat{\rho}_1^B$  at finite  $g_{AB}$ , for a)  $g_{AA} = 0.5$ , b)  $g_{AA} = 3.0$  and c)  $V = 500$  and varying majority-impurity coupling  $g_{AB}$  and the lattice depth  $V$  or the interaction strength of the majority atoms  $g_{AA}$ . All quantities are expressed in box units with characteristic length  $R^* = L$  and energy  $E^* = \hbar^2/(mL^2)$  while  $L$  is the extension of the box trap.

## B. Entropy measures for quantifying the degree of correlations

As we have seen in the previous section, an initially disentangled composite system may be drastically influenced by the intercomponent coupling. However, it is far from obvious to which extent the correlations are actually involved when the ground state undergoes structural changes [76]. For instance, a strongly interacting ground state may in fact just represent a different disentangled state or a state seemingly unaffected by the coupling may feature substantial correlations which guarantee its robustness. To investigate these intriguing possibilities we perform a further classification based on the degree of inter-particle correlations.

To quantify the degree of correlations in our impurity system we use the von-Neumann entropy of the reduced density operators [77]. Here, we distinguish between the *entanglement* entropy  $S_{vN}$  of the reduced density oper-

ator  $\hat{\rho}^\sigma$  of species  $\sigma$  [9, 45] and the *fragmentation* entropy  $S_{vN}^\sigma$  of the reduced one-body density operator  $\hat{\rho}_1^\sigma$  of species  $\sigma$  [51, 78, 79]. The former,  $\hat{\rho}^\sigma$ , is obtained by tracing the density operator  $\hat{\rho}$  of the composite many-body system over one of the species, while the latter,  $\hat{\rho}_1^\sigma$ , by additionally tracing  $\hat{\rho}^\sigma$  over all of the particles of the remaining component except one. In the presence of correlations the resulting reduced density operator will describe a mixed state. The entanglement entropy is caused by intercomponent correlations whereas the fragmentation entropy is primarily a signature of intracomponent ones, though it can be greatly impacted once the intercomponent correlations become dominant. Explicitly, the entanglement and fragmentation entropies are given as:

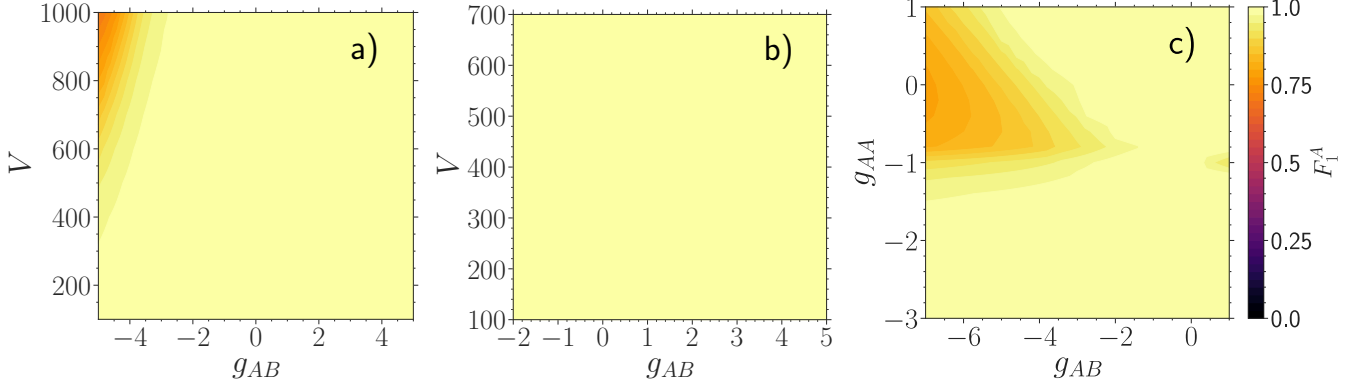


Figure 3. Fidelity  $F_1^A = F(\hat{\rho}_1^A, \hat{\rho}_1^A(g_{AB} = 0))$  between mixed states characterizing a majority particle when the medium is disentangled  $\hat{\rho}_1^A(g_{AB} = 0)$  and entangled  $\hat{\rho}_1^A$  with the impurity atom, for a)  $g_{AA} = 0.5$ , b)  $g_{AA} = 3.0$  and c)  $V = 500$  as a function of the majority-impurity coupling  $g_{AB}$  and the lattice depth  $V$  (a,b) or the interaction strength of the majority atoms  $g_{AA}$  (c). All quantities are provided in box units of characteristic length  $R^* = L$  and energy  $E^* = \hbar^2/(mL^2)$  with  $L$  being the extension of the box trap.

$$S_{vN} = -\text{tr}(\hat{\rho}^\sigma \ln \hat{\rho}^\sigma) = -\sum_{i=1}^S \lambda_i \ln \lambda_i \quad (7)$$

$$\text{with } \hat{\rho}^\sigma = \text{tr}_{\bar{\sigma}}(\hat{\rho}) = \sum_{i=1}^S \lambda_i |\Psi_i^\sigma\rangle \langle \Psi_i^\sigma|,$$

$$S_{vN}^\sigma = -\text{tr}(\hat{\rho}_1^\sigma \ln \hat{\rho}_1^\sigma) = -\sum_{i=1}^{s_\sigma} n_i^\sigma \ln n_i^\sigma \quad (8)$$

$$\text{with } \hat{\rho}_1^\sigma = \text{tr}_{N_\sigma-1}(\hat{\rho}^\sigma) = \sum_{i=1}^{s_\sigma} n_i^\sigma |\Phi_i^\sigma\rangle \langle \Phi_i^\sigma|.$$

In these expressions,  $\lambda_i$  and  $|\Psi_i^\sigma\rangle$  denote the natural populations and natural orbitals of the spectrally decomposed  $\hat{\rho}^\sigma$ , while  $n_i^\sigma$  and  $|\Phi_i^\sigma\rangle$  are the natural populations and natural orbitals of the spectrally decomposed  $\hat{\rho}_1^\sigma$  [59, 71]. Also,  $S$  and  $s_\sigma$  are the number of species orbitals and single-particle functions respectively,  $N_\sigma$  is the number of  $\sigma$  component particles and  $\sigma \neq \bar{\sigma}$ .

In the following, we display the species entanglement  $S_{vN}$  from Eq. (7) [Fig. 4] and the majority fragmentation  $S_{vN}^A$  from Eq. (8) [Fig. 5] as a function of the majority-impurity coupling  $g_{AB}$  and the lattice depth  $V$  or the interaction strength of the majority atoms  $g_{AA}$ . In case the entanglement entropy  $S_{vN}$  is close to zero, the corresponding subsystems are to a very good approximation disentangled. Thus, making a SMF ansatz in Eq. (2) would greatly facilitate numerical calculations while providing quantitatively good results for physical observables. On the other hand, already moderate values of entanglement may have an impact on some physical quantities with measurable differences to the SMF approximation. Regarding the fragmentation entropy of interacting majority atoms  $S_{vN}^A$  it is highly non-trivial to predict how their intrinsic mixedness, caused by the

intra-particle interactions  $g_{AA}$ , can be changed by the intercomponent coupling  $g_{AB}$ .

#### 1. Weakly repulsive interacting majority component

For a weakly interacting majority component with  $g_{AA} = 0.5$ , the entanglement entropy  $S_{vN}$  [Fig. 4a] displays two different behaviors depending on the sign of the coupling strength. For positive  $g_{AB}$  it increases gradually with increasing coupling strength  $g_{AB}$ , with the build-up being faster for a deeper lattice [51]. This is related to the onset of phase separation taking place sooner for a deeper lattice with increasing  $g_{AB}$  (see also the discussion in Section IV C). Turning to negative  $g_{AB}$  the entanglement entropy first grows gradually with decreasing coupling strength  $g_{AB}$ , but then, for larger  $V$  below some threshold value, the entanglement reduces to almost zero ( $g_{AB} < -4$  and  $V > 600$ ). Apart from the above mentioned pattern the overall behavior of  $S_{vN}$  in Fig. 4a is very similar to the one observed in the corresponding many-body fidelity [Fig. 1a].

The fragmentation entropy of the majority component  $S_{vN}^A$  [Fig. 5a] at  $g_{AB} = 0$  is larger for a deeper lattice. The reason is that the ratio of the intraspecies interaction energy and the single-particle energy of the majority component increases with a larger  $V$  or  $g_{AA}$ . In the limit of an infinitely deep lattice or an infinitely strong intraspecies repulsion we expect full fermionization, meaning that the one-body density operator becomes a mixed state with a uniform distribution of natural orbitals and the fragmentation entropy of the majority component reaches the value  $\ln(N_A) \approx 1.6$ . However, we observe that we are operating far away from that limit, since  $\max S_{vN}^A < 0.4$ .

At positive  $g_{AB}$ , as the entanglement entropy  $S_{vN}$  builds up [Fig. 4a], the fragmentation entropy  $S_{vN}^A$  of the majority component at  $g_{AB} = 0$  is more robust to varia-

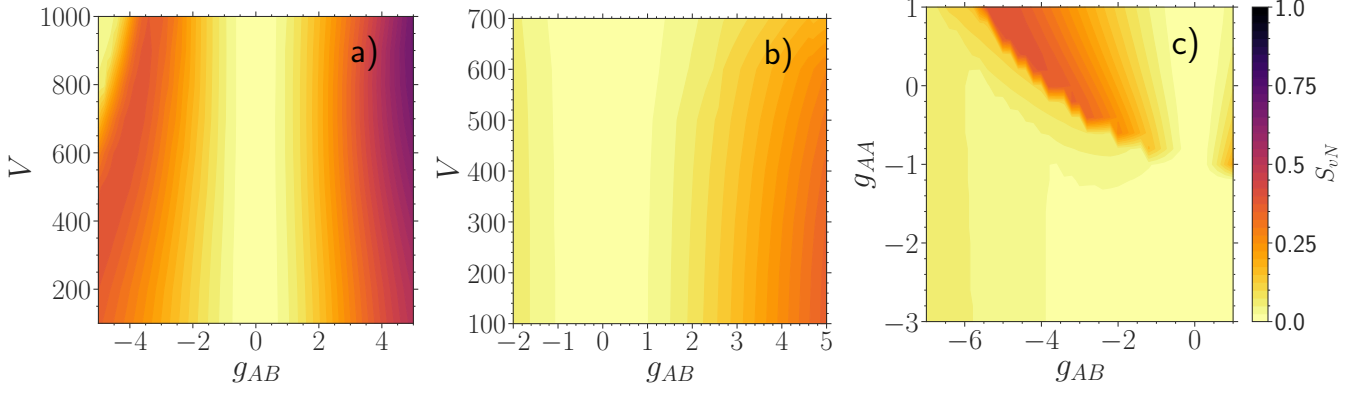


Figure 4. Entanglement entropy  $S_{vN}$ , see Eq. (7), for a)  $g_{AA} = 0.5$ , b)  $g_{AA} = 3.0$  and c)  $V = 500$  with varying majority-impurity coupling  $g_{AB}$  and the lattice depth  $V$  (a,b) or the interaction strength of the majority atoms  $g_{AA}$  (c). All quantities are given in box units with characteristic length  $R^* = L$  and energy  $E^* = \hbar^2/(mL^2)$  with  $L$  denoting the extension of the box trap.

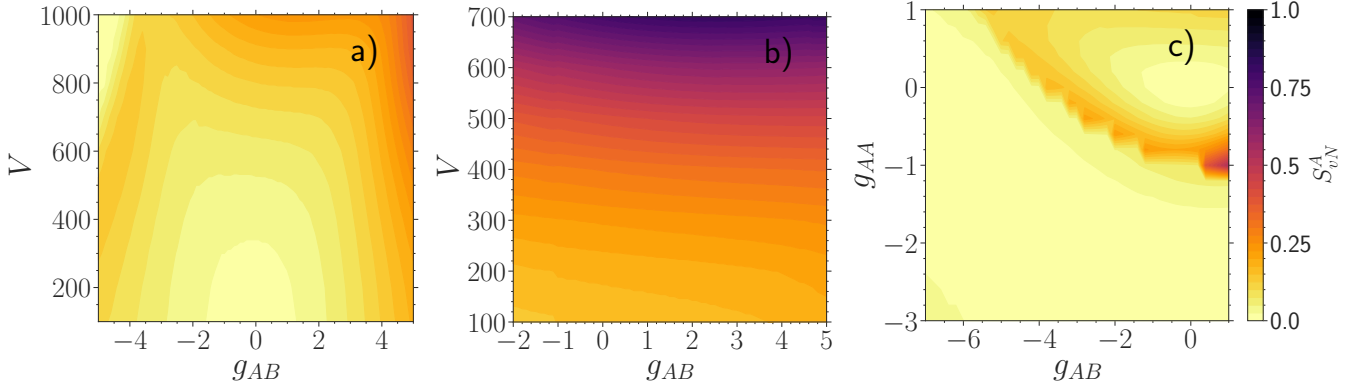


Figure 5. Fragmentation entropy  $S_{vN}^A$ , see Eq. (8), for a)  $g_{AA} = 0.5$ , b)  $g_{AA} = 3.0$  and c)  $V = 500$  with respect to the majority-impurity coupling  $g_{AB}$  and the lattice depth  $V$  (a,b) or the interaction strength of the majority atoms  $g_{AA}$  (c). All quantities are provided in terms of box units with characteristic length  $R^* = L$  and energy  $E^* = \hbar^2/(mL^2)$  while  $L$  denotes the extension of the box trap.

tions of  $g_{AB}$  at deeper lattice depths compared to shallow lattices [Fig. 5a]. Once the entanglement becomes strong enough to overcome intracomponent correlations, the fragmentation entropy of the majority atoms starts to increase with a fast rate (e.g.  $V = 1000$ ,  $g_{AB} > 4$ ). At negative  $g_{AB}$ , if the medium features a small fragmentation entropy at  $g_{AB} = 0$  ( $V < 900$ ), then  $S_{vN}^A$  rises first with decreasing  $g_{AB}$ , reaches a local maximum and finally drops to very small values at a sufficiently strong coupling strength. In contrast, if the fragmentation entropy of the decoupled majority component has already reached a moderate magnitude ( $V > 900$ ), then the initial fragmentation is gradually reduced with decreasing  $g_{AB}$ , until finally both entropies become negligibly small ( $g_{AB} < -4$ ). Once that happens, the resulting many-body state becomes to a good approximation a disentangled composite state with a condensed majority component.

## 2. Moderately repulsive interacting majority component

The entanglement entropy  $S_{vN}$  of a moderately interacting majority medium at  $g_{AA} = 3.0$  in Fig. 4b displays the same qualitative behavior as the many-body fidelity  $F_{mb}$  shown in Fig. 1b. Contrary to  $g_{AA} = 0.5$  the entanglement is overall less pronounced and builds up faster at shallow lattice depths instead. Such a comparatively weak entanglement leaves only a minor imprint on the fragmentation of the majority component  $S_{vN}^A$ , see Fig. 5b, manifested as a weak dependence on the coupling  $g_{AB}$ . The fragmentation of the majority species is substantial compared to  $g_{AA} = 0.5$  Fig. 5a at the same lattice depth. Nevertheless, the fermionization limit is not yet reached, since  $\max S_{vN}^A \approx 0.8$ . The intercomponent correlations are not strong enough to overcome the intraspecies ones in accordance with the robustness of the majority component observed on the one-body level in Fig. 3b. From this we expect a rather small impact of

entanglement on observables, which depend solely on the majority particle distribution.

### 3. Attractively interacting majority component

Finally, we analyze the dependence of the above-described entropy measures on the intraspecies interaction strength  $g_{AA}$  for a moderately deep lattice depth  $V = 500$  [Fig. 4c and Fig. 5c]. Since repulsive interactions have been already amply covered, we here concentrate on negative  $g_{AA}$  and  $g_{AB}$ .

As it can be readily seen, there is a parameter sector at  $g_{AB} < 0$  and  $g_{AA} > -1$  containing high values for the entanglement entropy  $S_{vN}$  [Fig. 4c]. This sector displays a similar behavior to  $S_{vN}$  in Fig. 4a at negative couplings, namely starting from the decoupled regime, the entanglement grows with decreasing  $g_{AB}$ , only to drastically decrease below some negative threshold value of  $g_{AB}$ . This threshold for  $g_{AB}$  lies at lower values the higher the intracomponent interaction strength  $g_{AA}$  is. We find that this abrupt decay of  $S_{vN}$  coincides with the one observed in the many-body fidelity  $F_{mb}$  [Fig. 1c]. This suggests that the disappearance of intercomponent correlations leads to an increased susceptibility of the system to  $g_{AB}$  variation. The other decay region, present in  $F_{mb}$  at  $g_{AA} \approx -1$  and negative  $g_{AB}$ , is missing in the entanglement entropy  $S_{vN}$ . From this we infer that it can be understood within the SMF picture. Additionally, there is also another much smaller sector characterized by a high entanglement entropy at  $g_{AB} > 0$  and  $g_{AA} \approx -1$ . It is directly related to structural changes observed in  $F_{mb}$  and  $F_1^A$  at the same values [Fig. 1c and Fig. 3c], which would have been absent in the SMF picture. Apart from that, below  $g_{AA} < -1$  the entanglement entropy among the components is either absent or of minor relevance.

Previously, we have mentioned that an isolated majority species, which interacts repulsively ( $g_{AA} > 0$ ), features a higher degree of fragmentation the larger  $g_{AA}$  is. In the case of attractive interactions ( $g_{AA} < 0$ ), however, the situation is different. Namely, starting from  $g_{AA} = 0$  the fragmentation entropy tends first to increase with decreasing  $g_{AA}$ , but then decreases up to the point of describing approximately a condensed state again [see Fig. 5c at  $g_{AB} = 0$ ]. Regarding the impact of the intercomponent coupling  $g_{AB}$  on  $S_{vN}^A$  we observe overall very similar patterns as for the entanglement entropy  $S_{vN}$  [Fig. 4c]. Regions where both entropic measures  $S_{vN}$  and  $S_{vN}^A$  are of small magnitude remind of the corresponding sectors in Fig. 4a and Fig. 5a at  $V > 800$  and  $g_{AB} < -4$ .

## C. Single- and two-particle density distributions

The measures of fidelity and entropy discussed in the previous sections are very useful in identifying parameter regions being substantially impacted and/or highly correlated indicating regimes of high interest for further investigation. However, they do not provide insights into the actually undergoing processes. To get a better understanding we ask for the impact on measurable quantities such as the one-body and two-body density distribution functions, which can be accessed by fluorescence imaging with a quantum gas microscope [80–84].

In the following,  $\rho_1^\sigma(z)$  describes the probability density to find a single particle of species  $\sigma$  at position  $z$ , while  $\rho_2^{\sigma\bar{\sigma}}(z_1, z_2)$  denotes the probability density to simultaneously measure one particle of species  $\sigma$  at position  $z_1$  and another one of the same or different species  $\bar{\sigma}$  at position  $z_2$ . The expectation value of any local observable depending on up to two degrees of freedom can be evaluated as an overlap integral with the appropriate probability density. Since many local observables often depend only on the distance between the particles, i.e.  $O(z_1, z_2) = O(z_1 - z_2)$ , we replace  $\rho_2^{\sigma\bar{\sigma}}(z_1, z_2)$  by the probability density  $\rho_r^{\sigma\bar{\sigma}}(r)$  to measure two particles belonging to the same or different species at a relative distance  $r$  independent of their individual positions. To this end we perform a coordinate transformation  $R = (z_1 + z_2)/2$  and  $r = z_1 - z_2$  giving the following identity:

$$\int \rho_2^{\sigma\bar{\sigma}}(z_1, z_2) dz_1 dz_2 = \int \rho_r^{\sigma\bar{\sigma}}(r, R) dr dR. \quad (9)$$

Then we define:

$$\rho_r^{\sigma\bar{\sigma}}(r) = \int \rho_2^{\sigma\bar{\sigma}}(r, R) dR. \quad (10)$$

Our first goal here is to investigate how the above mentioned quantities are affected in parameter sectors displaying strong susceptibility to structural changes identified in Section IV A and, in particular, whether the density distributions are capable to capture the undergoing changes in the many-body state.

Our second goal is to extract the impact of the entanglement. To this end we compare the above density distributions obtained from the variational ML-X calculations to the ones where the SMF ansatz is assumed. The latter will be distinguished by a tilde sign placed on top of the corresponding quantities. In the following, we shall evince that a large entanglement entropy identified in Section IV B has indeed a notable impact, but not always on all of the above mentioned density distributions. Thus, it may enhance or impede the effects coming from the induced SMF potential, such as phase separation and localization, or affect the bunching properties of the majority component.



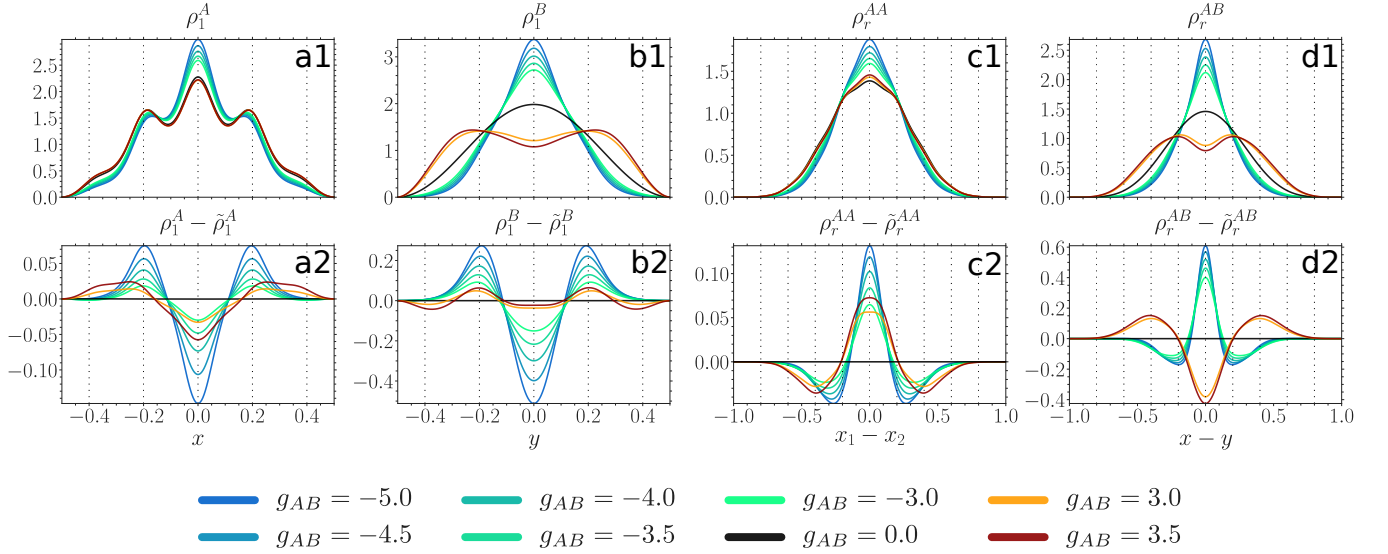


Figure 6. Upper panels: one-body probability densities  $\rho_1^A(x)$ ,  $\rho_1^B(y)$  [Eq. (4)] and distance probability distributions  $\rho_r^{AA}(x_1 - x_2)$ ,  $\rho_r^{AB}(x - y)$  [Eq. (10)] at  $g_{AA} = 0.5$ ,  $V = 100$  and for various values of  $g_{AB}$  (see legend). Lower panels: difference between probability densities obtained from the variational ML-X simulations and the SMF ansatz, the latter distinguished by a tilde sign. All quantities are given in box units with characteristic length  $R^* = L$  and energy  $E^* = \hbar^2/(mL^2)$  with  $L$  being the extension of the box trap.

### 1. Weakly repulsive interacting majority component

For a shallow lattice ( $V = 100$ ) we observe in Fig. 6 that the majority component (panel a1) at  $g_{AB} = 0$  occupies mainly the *central* site (at  $z = 0$ ) and the two *intermediate* ones (at  $z = \pm 0.2$ ), while  $\rho_r^{AA}$  (panel c1) features an almost Gaussian shape due to weak intraspecies correlations. At moderate positive couplings ( $g_{AB} > 3$ ) both quantities are only slightly affected in accordance with the robustness of  $F_1^A$  in this interaction regime [Fig. 3a]. At moderate negative couplings ( $g_{AB} < -3$ ) both  $\rho_1^A$  and  $\rho_r^{AA}$  shrink with decreasing  $g_{AB}$  indicating an increased bunching tendency of the majority atoms towards the central lattice site. The impact of entanglement here is moderate. It leads to an increased probability for the majority component to occupy the two intermediate sites, while disfavoring the central site (panel a2). Thus, it acts as an inhibitor of localization at negative  $g_{AB}$  and counteracts changes induced by the SMF potential at positive  $g_{AB}$ . Furthermore, entanglement favors bunching of the majority particles independent of the sign of the coupling (panel c2).

The decoupled impurity particle (panel b1) occupies the ground state of the box potential. At moderate positive couplings it develops two humps and forms a shell around the majority component density, a signature of phase separation [45, 62] further confirmed by the appearance of two humps in  $\rho_r^{AB}$  (panel d1). At negative couplings  $\rho_1^B$  and  $\rho_r^{AB}$  shrink with decreasing  $g_{AB}$  accumulating around the trap center. The entanglement favors the process of phase separation at positive couplings and bunching between the two species at negative

couplings (panel d2), while slowing down the shrinking of  $\rho_1^B$  at negative coupling (panel b2). We also remark that upon reaching a certain threshold value of  $g_{AB} > 4$ , the SMF solution experiences breaking of parity symmetry, causing substantial differences to the many-body symmetry-preserving solution (not shown).

For a deep lattice ( $V = 1000$ ) in Fig. 7 the majority component (panel a1) at  $g_{AB} = 0$  displays an almost uniform distribution over all the lattice sites, while  $\rho_r^{AA}$  (panel c1) features a multi-hump structure due to stronger intraspecies correlations [cf. Fig. 5a]. At moderate positive couplings ( $g_{AB} > 3$ ) the width of  $\rho_1^A$  and  $\rho_r^{AA}$  is only slightly increased, again in accordance with the robustness of  $F_1^A$  [Fig. 3a]. Thus, the majority component, experiencing the presence of a repelling impurity atom, shows a slight enhancement of the already present delocalization over the lattice. At moderate negative couplings ( $g_{AB} < -3$ ) both  $\rho_1^A$  and  $\rho_r^{AA}$  shrink with decreasing  $g_{AB}$  to the extent where all atoms occupy predominantly only the central site ( $g_{AB} < -4$ ). Such a large difference to the non-interacting ground state is in accordance with the observations made in  $F_1^A$  [Fig. 3a].

The impact of entanglement is structurally different compared to a shallow lattice (panels a2 and c2). At positive couplings, the entanglement greatly increases the probability for the majority atoms to be found at the central site, while decreasing the probability at *outer* sites ( $z = \pm 0.4$ ) and being indifferent to the intermediate sites (panel a2). Additionally, it favors the bunching of the majority particles at the same or neighboring sites and disfavors them being more than two sites apart (panel c2). At negative couplings, it acts in a similar

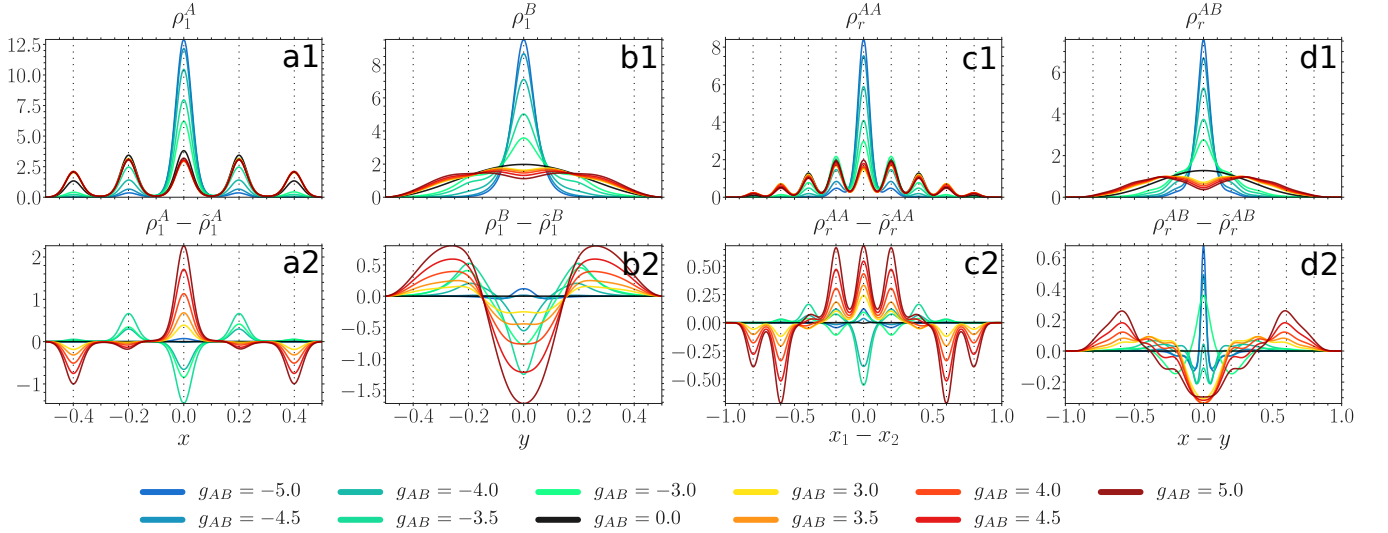


Figure 7. Upper panels: one-body probability densities  $\rho_1^A(x)$ ,  $\rho_1^B(y)$  [Eq. (4)] and distance probability distributions  $\rho_r^{AA}(x_1 - x_2)$ ,  $\rho_r^{AB}(x - y)$  [Eq. (10)] at  $g_{AA} = 0.5$ ,  $V = 1000$  and for various values of  $g_{AB}$  (see legend). Lower panels: difference between probability densities obtained from many-body ML-X calculations and SMF ansatz, the latter distinguished by a tilde sign. All quantities are given in box units with characteristic length  $R^* = L$  and energy  $E^* = \hbar^2/(mL^2)$  with  $L$  denoting the extension of the box trap.

way as in the case of shallow lattices, except that for a sufficiently strong coupling strength ( $g_{AB} < -4$ ), where both entropy measures are of small magnitude [see Figs. 4 and 5a], the SMF ansatz is in good accordance with the many-body solution.

The impurity particle (panel b1) at positive couplings ( $g_{AB} > 3$ ) first develops two humps, but then as the coupling increases, the relative distance between those peaks grows, while the humps themselves become flatter. There is a strong signature of an onset of a four-peak structure at  $g_{AB} = 5$ . This is in accordance with the increasing relative distance between the species (panel d1) and the fact that the majority atoms are distributed uniformly over all the lattice sites in contrast to  $g_{AA} = 0.5$ , where the majority component was occupying mainly the central and the intermediate sites. At negative couplings ( $g_{AB} < -3$ )  $\rho_1^B$  and  $\rho_r^{AB}$  shrink with decreasing  $g_{AB}$ .

The entanglement favors the process where the impurity atom moves from the box center to its boundaries independently of the sign of the coupling (panel b2). At  $g_{AB} < -4.0$  it plays only a minor role, the same as for the majority component. Regarding  $\rho_r^{AB}$ , at positive couplings the entanglement favors the process of phase separation by pushing the impurity particle more than two sites apart from a majority atom (panel d2). At negative couplings it enhances the bunching between the two species, even when the entanglement entropy is very small (e.g. at  $g_{AB} = -5.0$ ).

## 2. Moderately repulsive interacting majority component

Considering our findings regarding fidelity and entropy measures we investigate here only shallow lattices at positive couplings (Fig. 8), where the structural changes caused by the coupling and the entanglement entropy  $S_{vN}$  may have a sizable impact on density distributions. The decoupled density of the majority component (panel a1) has three pronounced humps at the *central* ( $z = 0$ ) and *intermediate* sites ( $z = \pm 0.2$ ). The profile is overall more spread compared to a weakly interacting majority [cf. Fig. 6 panel a1]. Indeed, it is most beneficial for two particles to occupy neighboring sites (see the two humps in panel c1). The majority component gets only a weak feedback from the presence of a repulsive impurity atom, even at coupling strengths comparable to  $g_{AA}$  in accordance with the robustness of  $F_1^A$  in Fig. 3b. The role of the entanglement is also rather weak, though qualitatively different to  $g_{AA} = 0.5$  in Fig. 6. Thus, it increases the probability for the majority particle to be found at the region enclosed between the two intermediate sites, while decreasing the probability to be detected outside of that region (panel a2). Furthermore, it favors particle distances of a half lattice constant ( $a_l = 0.2R^*$ ) (panel c2).

The impurity particle (panel b1) experiences phase separation similar to Fig. 6 (panel b1), i.e., upon increasing  $g_{AB}$  it develops two humps with a minimum at the trap center. Then, those humps separate and flatten, until finally they would form a four-hump structure with three local minima located at the position of the three peaks in the majority component density (compare to

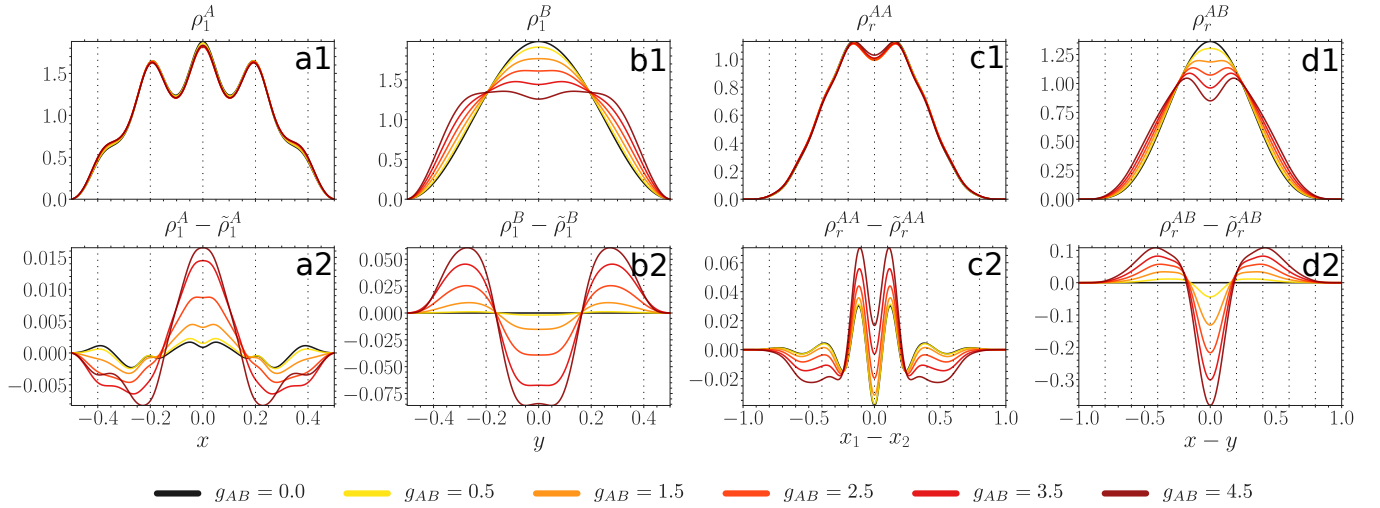


Figure 8. Upper panels: one-body probability densities  $\rho_1^A(x)$ ,  $\rho_1^B(y)$  [Eq. (4)] and distance probability distributions  $\rho_r^{AA}(x_1 - x_2)$ ,  $\rho_r^{AB}(x - y)$  [Eq. (10)] at  $g_{AA} = 3.0$ ,  $V = 100$  and for different values of  $g_{AB}$  (see legend). Lower panels: difference between probability densities obtained from the many-body ML-X calculations and SMF ansatz, the latter distinguished by a tilde sign. All quantities are provide in terms of box units with characteristic length  $R^* = L$  and energy  $E^* = \hbar^2/(mL^2)$  while  $L$  is the extension of the box trap.

panel a1). The separation between the species is again clearly manifested as two humps in  $\rho_r^{AB}$  with favored distance of a lattice constant ( $a_l = 0.2R^*$ ) (panel d1). The entanglement affects the impurity atom in quite an opposite way when compared to the majority component (panel b2), i.e., it decreases the probability for the impurity atom to be found at the region enclosed between the two intermediate sites, while increasing the probability to lie outside of that region. Additionally, similar to the behavior at weaker  $g_{AA}$  [cf. Fig. 6 panel d2], the entanglement accelerates the phase separation process (panel d2).

### 3. Attractively interacting majority component

Finally, we concentrate on negative intraspecies interactions  $g_{AA}$ , namely a weak negative  $g_{AA} = -0.4$  at negative  $g_{AB}$  [Fig. 9], contained in the parameter sector with substantial entanglement entropy [Fig. 4c].

In Fig. 9 a decoupled majority atom where  $g_{AB} = 0$  is localized at the *central* ( $z = 0$ ) and *intermediate* ( $z = \pm 0.2$ ) wells (panel a1). Even though the majority atoms are attracted to each other, the probability to be one or even two wells apart is still sizable (panel c1). With decreasing  $g_{AB}$  both  $\rho_1^A$  and  $\rho_r^{AA}$  shrink to a Gaussian. The impact of entanglement is quite different compared to the previously considered cases. Thus, at  $g_{AB} > -4.8$  the entanglement slows down the process of  $\rho_1^A$  localization at the central well (panel a2). The strongest impact is reached around  $g_{AB} \approx -2.4$ , where the entanglement entropy is largest for the given value of intracomponent interaction  $g_{AA} = -0.4$  [Fig. 4c]. Below  $g_{AB} < -4.8$ , as the entanglement entropy suddenly

drops, so does the difference to the SMF ansatz. The intercomponent correlations favor clustering of the majority atoms at  $-2.4 < g_{AB} < 0$  and  $g_{AB} < -4.2$ , whereas at  $-4.2 < g_{AB} < -2.4$ , where the entanglement entropy is largest, they inhibit the clustering (panel c2).

The impurity density  $\rho_1^B$  shows a similar behavior as the majority component density (panel b1), also in terms of the role of the entanglement (panel b2). The width of  $\rho_r^{AB}$  shrinks with decreasing  $g_{AB}$  (panel d1), while the entanglement enhances the bunching between the two species (panel d2).

## V. QUENCH INDUCED TUNNELING DYNAMICS

Having analyzed in detail the ground state properties of our system, we subsequently study the dynamical response of a single impurity coupled to a lattice trapped species upon quenching the interspecies interaction strength  $g_{AB}$ . To this end we prepare the system in its ground state for  $V = 500$ ,  $g_{AB} = 6.0$  and  $g_{AA} = 0.5$ , leading to the formation of a two-fold degeneracy in the ground state and the two species phase separate [45]. In this sense, the ground state one-body density is given by a superposition state of two parity-symmetry broken configurations, where the density of the first one is depicted in Fig. 10a and the second one corresponds to its parity-symmetric (with respect to  $x = 0$ ) counterpart. It is possible to remove this degeneracy in order to select any of the states in the respective degenerate manifold. Technically, this is done by applying a small asymmetry, e.g. a tilt, to the lattice potential, thereby breaking the parity symmetry and energetically favoring one of the

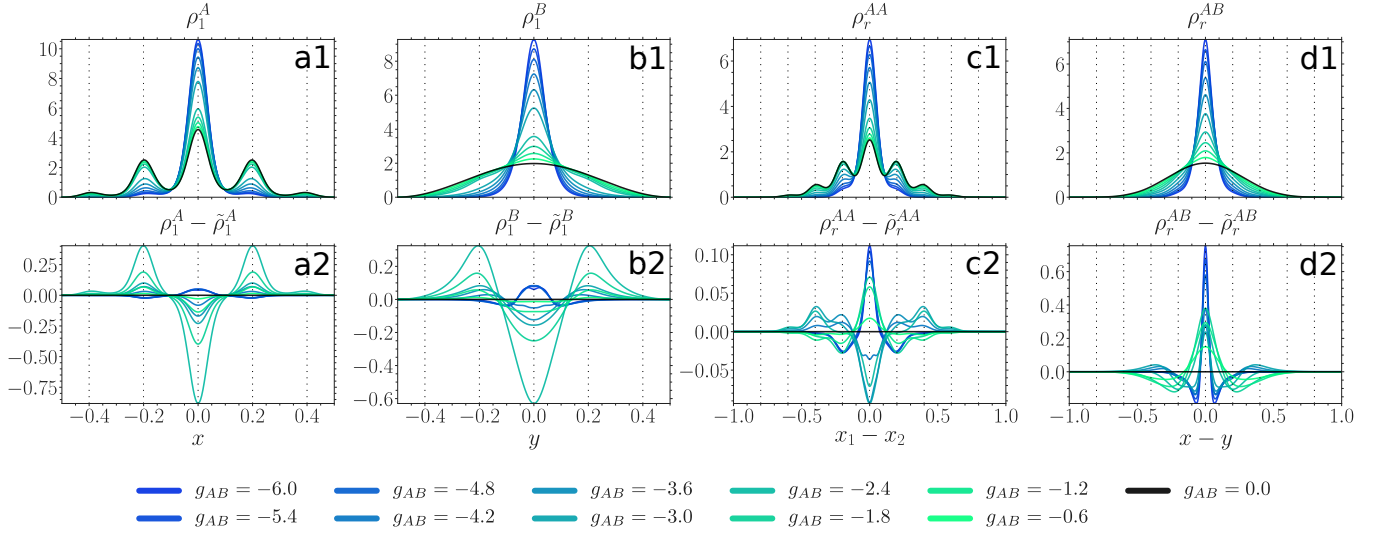


Figure 9. Upper panels: one-body probability densities  $\rho_1^A(x)$ ,  $\rho_1^B(y)$  [Eq. (4)] and distance probability distributions  $\rho_r^{AA}(x_1 - x_2)$ ,  $\rho_r^{AB}(x - y)$  [Eq. (10)] at  $g_{AA} = -0.4$ ,  $V = 500$  and for various values of  $g_{AB}$  (see legend). Lower panels: difference between probability densities obtained from the variational ML-X simulations and SMF ansatz, the latter distinguished by a tilde sign. All quantities are expressed in box units of characteristic length  $R^* = L$  and energy  $E^* = \hbar^2/(mL^2)$  while  $L$  being the extension of the box trap.

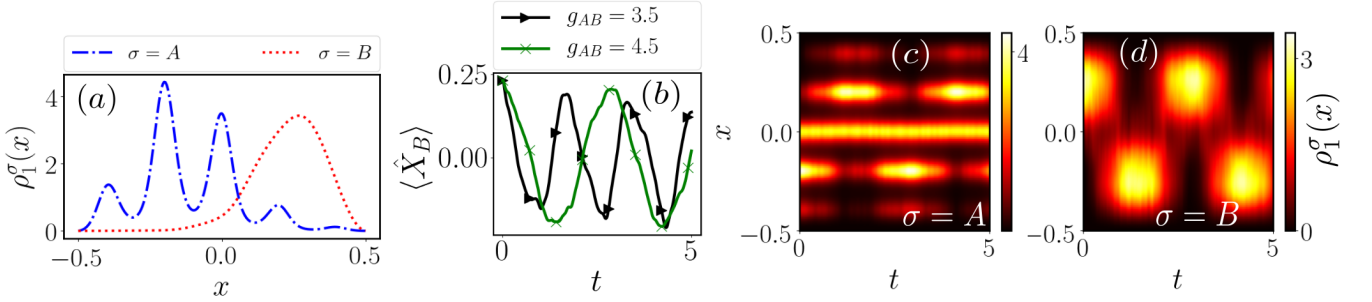


Figure 10. (a) One-body density  $\rho_1^\sigma(x)$  of the initial state configuration for  $V = 500$ ,  $g_{AA} = 0.5$  and  $g_{AB} = 6.0$  at  $t = 0$ . Temporal evolution of (b) the averaged position of the impurity  $\langle \hat{X}_B \rangle$  [see eq. (11)], (c) the one-body density of the majority species and (d) the one-body density of the impurity upon quenching the interspecies interaction strength to  $g_{AB} = 4.5$ .

above-mentioned states [49].

To trigger the dynamics starting from the initial state configuration illustrated in Fig. 10a we quench the interspecies interaction strength to a smaller value. As a representative example of the emergent tunneling dynamics of each species we present the temporal evolution of the corresponding one-body densities in Fig. 10c,d following a quench to  $g_{AB} = 4.5$ , while keeping fixed  $V = 500$  and  $g_{AA} = 0.5$ . In this case the impurity performs an oscillatory motion which is reminiscent of the tunneling of a particle in a double-well. This can be attributed to the lifting of the degeneracy for smaller interspecies interaction strengths. For a post-quench value of  $g_{AB} = 4.5$  the initially prepared state has a substantial overlap with the post-quench ground state and the first excited state such that in the course of the dynamics the system will oscillate between those two. This is similar to a single

particle in a double-well which is prepared as a superposition of the first doublet and undergoes a tunneling between the sites. Correspondingly, the majority species will undergo a collective tunneling in the lattice geometry [49, 52]. Thus, the probability distribution of a single majority species particle will oscillate between the initial distribution [Fig. 10a] and its parity-symmetric counterpart. Due to the repulsive nature of the interspecies coupling the two species move in opposite directions such that they end up in phase-separated configurations after half a period. Note that the oscillation period, being the energy gap between the two energetically lowest eigenstates of the post-quench Hamiltonian (not shown here), depends on the post-quench  $g_{AB}$ . This can be easily verified by monitoring the temporal evolution of the averaged



position of the impurity [13] which is defined as

$$\langle \hat{X}_B \rangle = \int_{-L/2}^{L/2} dx \rho_1^B(x) x. \quad (11)$$

For various post-quench  $g_{AB}$  we find that the impurity will occupy its parity-symmetric counterpart, reflected in the decrease of  $\langle \hat{X}_B \rangle$  towards negative values, while the oscillation decreases with smaller  $g_{AB}$  [Fig. 10b]. In order to gain insight into beyond mean-field effects we investigate the natural populations  $n_j^\sigma$  [see eq. (8)] which indicate the degree of fragmentation of the subsystem [9, 70]. For simplicity here we present the populations of the first two dominantly populated natural orbitals while using six orbitals in the actual calculations. The initial depletion of both subsystems is rather small, i.e.  $n_1^A \approx 0.996$  and  $n_1^B \approx 0.99$ , such that any decrease of these populations upon quenching  $g_{AB}$  is due to dynamical many-body effects. We find that for both subsystems dominantly two natural orbitals contribute during the dynamics [Fig. 11c,d], while the ones of the medium are less impacted by the quench. For the natural populations of the impurity signatures of an oscillation can be observed, where  $n_1^B$  initially decreases and revives back towards  $n_1^B \approx 0.99$ , while  $n_2^B$  initially increases and afterwards drops back to nearly zero. In order to attribute the occupation of the additional natural orbital to physical processes, we analyze the spatial distribution of the natural orbitals  $\Phi_j^B(x, t)$  [see eq. (8)] themselves focusing on the impurity [Fig. 11a,b]. In Fig. 11a we observe that the first natural orbital corresponds to the oscillatory behavior of the one-body density of the impurity, but lacking the smooth transition between the phase-separated configurations [see Fig. 10d]. The first natural orbital dominates during the dynamics and we can interpret its behavior as corresponding to the presence of the phase-separated density configurations. Consequently, the second natural orbital [Fig. 11b], resembling the mirror image of the first one, contributes to deviations from this solution. Due to its structure we can deduce that it is responsible for initiating the transport of the impurity, thereby allowing for the counterflow of the two species. Note that the presence of more than one natural orbital during the dynamics is a clear signature that mean-field theory would not provide an accurate description of the system dynamics. Hence, the fact that  $|\Phi_2^B\rangle$  is occupied is a manifestation of many-body effects, influencing the motion of both species.

## VI. SUMMARY AND OUTLOOK

In this work we analyze the static and dynamical properties of a few-body particle-imbalanced bosonic mixture at zero temperature. Importantly, the components are exposed to different one-dimensional external traps where the majority species is subject to a finite lattice potential while the single impurity is trapped in a box of

the same extension as the lattice. We study the response of the composite system upon the variation of majority-impurity coupling  $g_{AB}$  and majority component internal parameters being either the lattice depth  $V$  or the majority-majority interaction strength  $g_{AA}$ .

To quantify the response of static properties we employ the fidelity between two density operators describing ground states at zero and a finite intercomponent interaction  $g_{AB}$ . We contrast the response at the many-body to the single-particle level. We observe that the composite system is quite robust to the variation of the intercomponent interaction at strongly repulsive  $g_{AA}$ , while being fragile at strongly attractive  $g_{AB}$  and deep lattices  $V$  as well as when  $g_{AA}$  is weakly attractive and  $g_{AB}$  is strongly attractive. Upon comparison to the fidelities between the corresponding reduced one-body density operators of each component, we not only observe that each species is affected to a much smaller degree, but they also respond differently. Thus, for the impurity atom the deviation from the box ground state increases smoothly with increasing absolute value of  $g_{AB}$ , while the reduced density of the majority component remains very robust to  $g_{AB}$  variations except for the above mentioned parameter regions where the many-body fidelity exhibits significant structural changes in the ground state.

Next, we have been performing a further classification of our system based on entropy measures. Namely, we quantify the amount of entanglement and intraspecies correlations deposited in the binary mixture by evaluating the von-Neumann entropy of the respective subsystems. Interestingly, we find that our composite system is only weakly entangled for parameter regions which undergo substantial structural changes. Additionally, we observe that while the entanglement entropy continuously grows with increasing repulsive  $g_{AB}$ , it does not behave the same for attractive  $g_{AB}$ , where it reaches a local maximum at a finite value of  $g_{AB} < 0$ . Another peculiar observation is that the fragmentation entropy of the majority component undergoes a strong variation for parameter regions, where the fidelity measure does not show any evidence of majority particles being affected by the intercomponent interaction. Even though the mixed character of the reduced density of the medium suffers from substantial changes, it remains un-observable on the single-particle level.

To visualize our observations stemming from the fidelity measure we show the one-body density distributions of each component along with the probability distributions for two particles of the same or different species to be measured at a relative distance from each other. These quantities are usually accessible in state-of-the-art ultracold atom experiments and determine the expectation values of local one- and two-body observables. Indeed, strong deviations appearing in the fidelity at the single-particle level are also clearly visible in the corresponding one-body density. At positive couplings we observe an interspecies phase separation where the impurity is pushed to the box edges, while leaving the majority

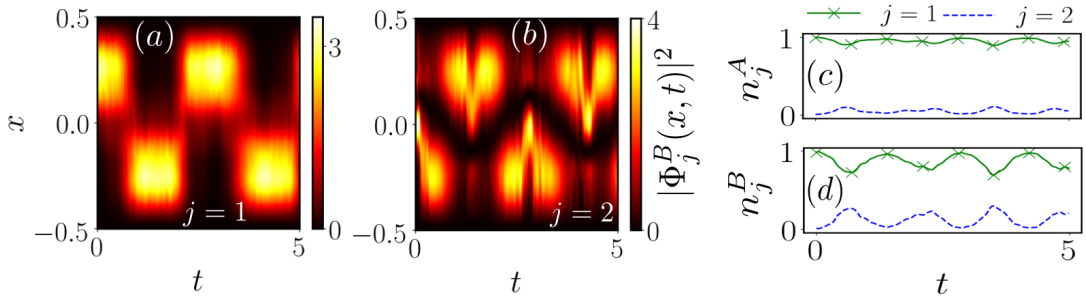


Figure 11. Temporal evolution of the density of (a) the first and (b) the second natural orbital  $\Phi_j^B(x, t)$  [see eq. (8)] of the impurity and (c), (d) the natural populations  $n_j^\sigma$  of both subsystems upon quenching the interspecies interaction strength  $g_{AB}$  of the ground state in Fig. 10a to  $g_{AB} = 4.5$ .

component intact. At negative couplings both components tend to increase their localization at the central well.

To further quantify our conclusions stemming from the entanglement measure we rely on the difference between the above probability distributions and the corresponding ones when assuming a disentangled state in our calculations. Again, we find strong deviations for parameters displaying high entanglement entropy values. Thus, at positive couplings the entanglement favors the process of phase separation, while at negative couplings it generally, but not always, counteracts the localization of both species.

Quenching the interspecies interaction strength we are able to induce a dynamical process which for the impurity is reminiscent of the tunneling of a single particle in a double well potential. This can be attributed to the lifting of the degeneracy for the corresponding post-quench Hamiltonian as well as the substantial overlap of the initial state configuration with the post-quench ground state and the first excited state. Due to the repulsive interspecies interaction also the majority species will undergo a tunneling in the lattice geometry such that the two species move in opposite directions, ending up in phase-separated configurations after half a period. We identify the presence of two dominant natural orbitals for the impurity species during the dynamics, where the first one corresponds to phase-separated configurations in the respective one-body density, while the second one resembles the mirror image of the first one. The presence of an additional natural orbital emphasizes the many-

body character of the dynamics, thereby influencing the motion of the impurity.

There are various promising research directions that are worth pursuing in the future. Indeed, the generalization of our findings for an increasing particle number in the medium or larger lattice potentials as well as the role of the lattice filling factor is desirable. Also, a more elaborated analysis on the possibly emerging impurity-medium bound states or the engineering of droplet-like configurations in such settings at strong intercomponent attractions would be important. Furthermore, it would be intriguing to study the persistence and possible alterations of the identified spatial configurations in the presence of finite temperature which will impact the coherence of the lattice bosons [85, 86]. Another perspective is to investigate the relevant radiofrequency spectrum [31, 42] in order to capture the emergent polaron properties including their lifetime, residue and effective mass especially in the attractive interaction regimes of bound state formation.

## ACKNOWLEDGMENTS

M. P. and K. K. gratefully acknowledge a scholarship of the Studienstiftung des deutschen Volkes. S. I. M. gratefully acknowledges financial support in the framework of the Lenz-Ising Award of the Department of Physics of the University of Hamburg.

- 
- [1] I. Bloch, J. Dalibard, and W. Zwerger, *Rev. Mod. Phys.* **80**, 885 (2008).
  - [2] I. Bloch, (Cambridge University Press, 2017) p. 253.
  - [3] T. Fukuhara, S. Sugawa, Y. Takasu, and Y. Takahashi, *Phys. Rev. A* **79**, 021601 (2009).
  - [4] K. Henderson, C. Ryu, C. MacCormick, and M. G. Boshier, *New J. Phys.* **11**, 043030 (2009).
  - [5] F. Serwane, G. Zürn, T. Lompe, T. Ottenstein, A. Wenz, and S. Jochim, *Science* **332**, 336 (2011).
  - [6] R. Schmied, J.-D. Bancal, B. Allard, M. Fadel, V. Scarani, P. Treutlein, and N. Sangouard, *Science* **352**, 441 (2016).
  - [7] C. Chin, R. Grimm, P. Julienne, and E. Tiesinga, *Rev. Mod. Phys.* **82**, 1225 (2010).
  - [8] T. Köhler, K. Góral, and P. S. Julienne, *Rev. Mod. Phys.* **78**, 1311 (2006).
  - [9] S. I. Mistakidis, G. C. Katsimiga, P. G. Kevrekidis, and P. Schmelcher, *New J. Phys.* **20**, 043052 (2018).

- [10] M. Pyzh and P. Schmelcher, *Phys. Rev. A* **102**, 023305 (2020).
- [11] D. S. Petrov and G. E. Astrakharchik, *Phys. Rev. Lett.* **117**, 100401 (2016).
- [12] L. Parisi and S. Giorgini, *arXiv:2003.05231* (2020).
- [13] J. Catani, G. Lamporesi, D. Naik, M. Gring, M. Inguscio, F. Minardi, A. Kantian, and T. Giamarchi, *Phys. Rev. A* **85**, 023623 (2012).
- [14] F. Meinert, M. Knap, E. Kirilov, K. Jag-Lauber, M. B. Zvonarev, E. Demler, and H.-C. Nägerl, *Science* **356**, 945 (2017).
- [15] S. I. Mistakidis, A. G. Volosniev, N. T. Zinner, and P. Schmelcher, *Phys. Rev. A* **100**, 013619 (2019).
- [16] L. P. Ardila and S. Giorgini, *Phys. Rev. A* **92**, 033612 (2015).
- [17] F. Grusdt, G. E. Astrakharchik, and E. Demler, *New J. Phys.* **19**, 103035 (2017).
- [18] H. Tajima and S. Uchino, *New J. Phys.* **20**, 073048 (2018).
- [19] A. S. Dehkharghani, A. G. Volosniev, and N. T. Zinner, *Phys. Rev. Lett.* **121**, 080405 (2018).
- [20] S. I. Mistakidis, A. G. Volosniev, and P. Schmelcher, *Phys. Rev. Research* **2**, 023154 (2020).
- [21] J. Takahashi, H. Tajima, E. Nakano, and K. Iida, *arXiv:2011.07911* (2020).
- [22] F. Brauneis, H.-W. Hammer, M. Lemesko, and A. G. Volosniev, *arXiv:2101.10958* (2021).
- [23] P. Massignan, M. Zaccanti, and G. M. Bruun, *Rep. Progr. Phys.* **77**, 034401 (2014).
- [24] R. Schmidt, M. Knap, D. A. Ivanov, J.-S. You, M. Cetina, and E. Demler, *Rep. Progr. Phys.* **81**, 024401 (2018).
- [25] T. Fukuhara, A. Kantian, M. Endres, M. Cheneau, P. Schauss, S. Hild, and D. Bellem, *Nat. Phys.* **9**, 235 (2013).
- [26] Z. Z. Yan, Y. Ni, C. Robens, and M. W. Zwierlein, *Science* **368**, 190 (2020).
- [27] F. Scazza, G. Valtolina, P. Massignan, A. Recati, A. Amico, A. Burchianti, C. Fort, M. Inguscio, M. Zaccanti, and G. Roati, *Phys. Rev. Lett.* **118**, 083602 (2017).
- [28] N. B. Jørgensen, L. Wacker, K. T. Skalmstang, M. M. Parish, J. Levinsen, R. S. Christensen, G. M. Bruun, and J. J. Arlt, *Phys. Rev. Lett.* **117**, 055302 (2016).
- [29] M. Cetina, M. Jag, R. S. Lous, I. Fritsche, J. T. Walraven, R. Grimm, J. Levinsen, M. M. Parish, R. Schmidt, M. Knap, and E. Demler, *Science* **354**, 96 (2016).
- [30] A. Wenz, G. Zürn, S. Murmann, I. Brouzos, T. Lompe, and S. Jochim, *Science* **342**, 457 (2013).
- [31] S. I. Mistakidis, G. M. Koutentakis, F. Grusdt, H. R. Sadeghpour, and P. Schmelcher, *arXiv:2011.13756* (2020).
- [32] S. I. Mistakidis, G. M. Koutentakis, G. C. Katsimiga, T. Busch, and P. Schmelcher, *New J. Phys.* **22**, 043007 (2020).
- [33] A. Boudjemâa, N. Guebli, M. Sekmane, and S. Khlifa-Karfa, *J. Phys.: Cond. Matt.* **32**, 415401 (2020).
- [34] L. A. P. Ardila, G. E. Astrakharchik, and S. Giorgini, *Phys. Rev. Research* **2**, 023405 (2020).
- [35] A. Camacho-Guardian, L. A. P. Ardila, T. Pohl, and G. M. Bruun, *Phys. Rev. Lett.* **121**, 013401 (2018).
- [36] K. Mukherjee, S. I. Mistakidis, S. Majumder, and P. Schmelcher, *Phys. Rev. A* **102**, 053317 (2020).
- [37] G. Bougas, S. I. Mistakidis, and P. Schmelcher, *arXiv:2009.08901* (2020).
- [38] H. Tajima, J. Takahashi, E. Nakano, and K. Iida, *Phys. Rev. A* **102**, 051302 (2020).
- [39] S. I. Mistakidis, F. Grusdt, G. M. Koutentakis, and P. Schmelcher, *New J. Phys.* **21**, 103026 (2019).
- [40] K. Mukherjee, S. I. Mistakidis, S. Majumder, and P. Schmelcher, *Phys. Rev. A* **101**, 023615 (2020).
- [41] F. Theel, K. Keiler, S. I. Mistakidis, and P. Schmelcher, *arXiv:2009.12147* (2020).
- [42] S. I. Mistakidis, G. C. Katsimiga, G. M. Koutentakis, T. Busch, and P. Schmelcher, *Phys. Rev. Research* **2**, 033380 (2020).
- [43] T. Lausch, A. Widera, and M. Fleischhauer, *Phys. Rev. A* **97**, 023621 (2018).
- [44] S. Palzer, C. Zipkes, C. Sias, and M. Köhl, *Phys. Rev. Lett.* **103**, 150601 (2009).
- [45] K. Keiler, S. I. Mistakidis, and P. Schmelcher, *arXiv:2004.12719* (2020).
- [46] A. Bohrdt, F. Grusdt, and M. Knap, *New J. Phys.* **22**, 123023 (2020).
- [47] Z. Cai, L. Wang, X. Xie, and Y. Wang, *Phys. Rev. A* **81**, 043602 (2010).
- [48] T. H. Johnson, S. R. Clark, M. Bruderer, and D. Jaksch, *Phys. Rev. A* **84**, 023617 (2011).
- [49] F. Theel, K. Keiler, S. I. Mistakidis, and P. Schmelcher, *New J. Phys.* **22**, 023027 (2020).
- [50] K. Keiler and P. Schmelcher, *New J. Phys.* **20**, 103042 (2018).
- [51] K. Keiler, S. Krönke, and P. Schmelcher, *New J. Phys.* **20**, 033030 (2018).
- [52] K. Keiler and P. Schmelcher, *Phys. Rev. A* **100**, 043616 (2019).
- [53] M. Bruderer, W. Bao, and D. Jaksch, *Europhys. Lett.* **82**, 30004 (2008).
- [54] T. Yin, D. Cocks, and W. Hofstetter, *Phys. Rev. A* **92**, 063635 (2015).
- [55] F. Grusdt, A. Shashi, D. Abanin, and E. Demler, *Phys. Rev. A* **90**, 063610 (2014).
- [56] C. Weber, S. John, N. Spethmann, D. Meschede, and A. Widera, *Phys. Rev. A* **82**, 042722 (2010).
- [57] S. Will, T. Best, S. Braun, U. Schneider, and I. Bloch, *Phys. Rev. Lett.* **106** (2011).
- [58] H. Tajima, J. Takahashi, S. I. Mistakidis, E. Nakano, and K. Iida, *arXiv:2101.07643* (2021).
- [59] L. Cao, V. Bolsinger, S. Mistakidis, G. Koutentakis, S. Krönke, J. Schurer, and P. Schmelcher, *The J. Chem. Phys.* **147**, 044106 (2017).
- [60] L. Cao, S. Krönke, O. Vendrell, and P. Schmelcher, *J. Chem. Phys.* **139**, 134103 (2013).
- [61] S. Krönke, L. Cao, O. Vendrell, and P. Schmelcher, *New J. Phys.* **15**, 063018 (2013).
- [62] S. I. Mistakidis, G. C. Katsimiga, G. M. Koutentakis, T. Busch, and P. Schmelcher, *Phys. Rev. Lett.* **122**, 183001 (2019).
- [63] A. C. Pflanzner, S. Zöllner, and P. Schmelcher, *J. Phys. B: At. Mol. and Opt. Phys.* **42**, 231002 (2009).
- [64] C. J. Myatt, E. A. Burt, R. W. Ghrist, E. A. Cornell, and C. E. Wieman, *Phys. Rev. Lett.* **78**, 586 (1997).
- [65] D. S. Hall, M. R. Matthews, J. R. Ensher, C. E. Wieman, and E. A. Cornell, *Phys. Rev. Lett.* **81**, 1539 (1998).
- [66] H.-J. Miesner, D. M. Stamper-Kurn, J. Stenger, S. Inouye, A. P. Chikkatur, and W. Ketterle, *Phys. Rev. Lett.* **82**, 2228 (1999).
- [67] P. Maddaloni, M. Modugno, C. Fort, F. Minardi, and M. Inguscio, *Phys. Rev. Lett.* **85**, 2413 (2000).
- [68] K. M. Mertes, J. W. Merrill, R. Carretero-González, D. J.

- Frantzeskakis, P. G. Kevrekidis, and D. S. Hall, *Phys. Rev. Lett.* **99**, 190402 (2007).
- [69] C. Becker, S. Stellmer, P. Soltan-Panahi, S. Dörscher, M. Baumert, E.-M. Richter, J. Kronjäger, K. Bongs, and K. Sengstock, *Nature Physics* **4**, 496 (2008).
- [70] A. U. J. Lode, C. Lévêque, L. B. Madsen, A. I. Streltsov, and O. E. Alon, *Rev. Mod. Phys.* **92**, 011001 (2020).
- [71] O. E. Alon, R. Beinke, and L. S. Cederbaum, arXiv:2101.11615 (2021).
- [72] R. Horodecki, P. Horodecki, M. Horodecki, and K. Horodecki, *Rev. Mod. Phys.* **81**, 865 (2009).
- [73] J. Light, I. Hamilton, and J. Lill, *J. Chem. Phys.* **82**, 1400 (1985).
- [74] A. Raab, *Chem. Phys. Lett.* **319**, 674 (2000).
- [75] R. Jozsa, *J. Mod. Opt.* **41**, 2315 (1994).
- [76] W. Wang, V. Penna, and B. Capogrosso-Sansone, *New J. Phys.* **18**, 063002 (2016).
- [77] I. Bengtsson and K. Życzkowski, (Cambridge University Press, 2017).
- [78] R. Roy, A. Gammal, M. C. Tsatsos, B. Chatterjee, B. Chakrabarti, and A. U. J. Lode, *Phys. Rev. A* **97**, 043625 (2018).
- [79] S. Bera, S. K. Haldar, B. Chakrabarti, A. Trombettoni, and V. K. B. Kota, *European Phys. J. D* **74**, 1 (2020).
- [80] W. S. Bakr, A. Peng, M. E. Tai, R. Ma, J. Simon, J. I. Gillen, S. Fölling, L. Pollet, and M. Greiner, *Science* **329**, 547 (2010).
- [81] J. F. Sherson, C. Weitenberg, M. Endres, M. Cheneau, I. Bloch, and S. Kuhr, *Nature* **467**, 68 (2010).
- [82] A. Omran, M. Boll, T. A. Hilker, K. Kleinlein, G. Salomon, I. Bloch, and C. Gross, *Phys. Rev. Lett.* **115**, 263001 (2015).
- [83] M. Hohmann, F. Kindermann, T. Lausch, D. Mayer, F. Schmidt, E. Lutz, and A. Widera, *Phys. Rev. Lett.* **118**, 263401 (2017).
- [84] M. Pyzh, S. Krönke, C. Weitenberg, and P. Schmelcher, *New J. Phys.* **21**, 053013 (2019).
- [85] F. Lingua, B. Capogrosso-Sansone, F. Minardi, and V. Penna, *Sc. Rep.* **7**, 1 (2017).
- [86] K. W. Mahmud, E. N. Duchon, Y. Kato, N. Kawashima, R. T. Scalettar, and N. Trivedi, *Phys. Rev. B* **84**, 054302 (2011).